J. Fluid Mech. (2024), *vol*. 980, A8, doi:10.1017/jfm.2023.1078

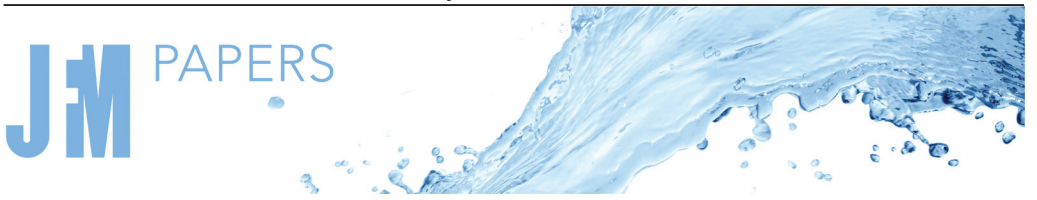

Characterization of very-large-scale motions in supersonic and hypersonic turbulent boundary layers

Ming Yu[1], SiWei Dong[1], QiLong Guo[1], ZhiGong Tang[2], XianXu Yuan[1,†] and ChunXiao Xu[3,†]

[1]State Key Laboratory of Aerodynamics, Mianyang 621000, PR China

[2]China Aerodynamics Research and Development Center, Mianyang 621000, PR China

[3]Key Laboratory of Applied Mechanics, Ministry of Education, Institute of Fluid Mechanics, Department of Engineering Mechanics, Tsinghua University, Beijing 100084, PR China

(Received 18 July 2023; revised 13 December 2023; accepted 13 December 2023)

Very-large-scale motions are commonly observed in moderate- and high-Reynolds-number wall turbulence, constituting a considerable portion of the Reynolds stress and skin friction. This study aims to investigate the behaviour of these motions in high-speed and high-Reynolds-number turbulent boundary layers at varying Mach numbers. With the aid of high-precision numerical simulations, numerical experiments and theoretical analysis, it is demonstrated that the very-large-scale motions are weakened in high-Mach-number turbulence at the same friction Reynolds numbers, leading to the reduction in turbulent kinetic energy in the outer region. Conversely, the lower wall temperature enhances the very-large-scale motions but shortens the scale separation between the structures in the near-wall and outer regions.

Key words: compressible turbulence, turbulent boundary layers

1. Introduction

In recent years, high-speed turbulent boundary layers have gained significant attention in fluid dynamic communities due to their potential applications in civilian transport within the aerospace industries (Leyva 2017; Tu *et al.* 2021; Theofilis, Pirozzoli & Martin 2022). Wind tunnel experiments (Williams *et al.* 2018; Segall *et al.* 2023) and high-fidelity numerical simulations (Duan, Beekman & Martin 2011; Pirozzoli 2011) have established numerous databases, providing enlightening insights into the scaling laws of mean and fluctuating velocity, pressure and temperature at varying Mach numbers

† Email addresses for correspondence: yuanxianxu@cardc.cn, xucx@tsinghua.edu.cn

and wall temperatures (Duan, Beekman & Martin 2010; Duan *et al.* 2011). Efforts have been made in the aspects including the integral transformations intended to collapse the mean velocities with those in incompressible flows (Trettel & Larsson 2016; Volpiani *et al.* 2020; Griffin, Fu & Moin 2021), the strong or generalized Reynolds analogy depicting the similarity and/or correlation between mean and fluctuating velocity and temperature (Huang, Coleman & Bradshaw 1995; Zhang *et al.* 2014), and the variation of turbulent flow quantities at the walls and the associated turbulent structures (Yu, Xu & Pirozzoli 2020; Yu *et al.* 2022*b*,*a*; Zhang *et al.* 2022). However, most previous studies have primarily focused on low-Reynolds-number flows. High-Reynolds-number effects, however, have not commonly been regarded as a subject of great importance in high-speed turbulence, for the high-Mach-number and high-Reynolds-number conditions rarely occur simultaneously, which is in stark contrast to the case of low-speed incompressible turbulence. It is only in recent years that new conceptual vehicles designed to fly at low altitudes have brought these two extreme conditions together.

Moderate and high-Reynolds-number turbulent boundary layers exhibit several typical features (Smits, McKeon & Marusic 2011), such as the separation of the inner and outer layers and hence a longer logarithmic layer (Marusic *et al.* 2013), the higher intensity of turbulent fluctuations in the inner and outer layers (Baars & Marusic 2020*a*,*b*; Chen & Sreenivasan 2021), and the manifestation of the streamwise elongated low-momentum regions in the outer layer with the spanwise length scale of boundary layer thickness δ, namely the very-large-scale motions (VLSMs) (Hutchins & Marusic 2007; Mathis, Hutchins & Marusic 2009; Jiménez 2018). Similar phenomena can be observed in high-speed flows as well, according to the previous experimental and numerical studies of Ganapathisubramani, Clemens & Dolling (2006) and Pirozzoli & Bernardini (2013), where direct numerical simulation (DNS) is performed at the free stream Mach number M_∞ (the ratio between the free stream velocity U_∞ and sound speed a_∞) of 2.0 and the friction Reynolds number Re_τ ($Re_\tau = \rho_w u_\tau \delta/\mu_w$, with ρ_w the wall density, u_τ the friction velocity defined by the wall shear stress τ_w and wall density ρ_w, and μ_w the wall viscosity) up to 5600 and 4000, respectively. A recent study by Bross, Scharnowski & Kähler (2021) revealed that the characteristic length scales of the VLSMs are sensitive to the Mach number when the free stream transits from subsonic to supersonic flows, with the highest Mach number being 3.0. Cogo *et al.* (2022) and Huang, Duan & Choudhari (2022) extended the study of high-Reynolds-number turbulence to Mach numbers up to $M_\infty = 5.86$ over mildly cooling walls and $M_\infty = 11$ over cold walls, respectively. It is concluded that the VLSMs are also manifested at high Mach numbers, and there is a strong correlation between low-momentum and high-temperature regions. Decreasing the wall temperature results in a shorter separation between the small-scale motions in the near-wall region and the VLSMs in the outer layers. Although not pointed out directly in these studies, it can be observed in the figures reported that the peaks of the spectra in the outer layer, the direct statistical evidence of VLSMs, are lowered at higher Mach number flows at roughly the same Re_τ. The high-speed high-Reynolds-number wall-bounded turbulence has been considered in other flow configurations, such as channels (Modesti & Pirozzoli 2016; Yao & Hussain 2020, 2023), pipes (Modesti & Pirozzoli 2019) and square ducts (Modesti, Pirozzoli & Grasso 2019), which will not be included in the short literature review here due to the different features of heat transfer.

Linear stability analysis, such as the transient growth of optimal perturbations (Del Alamo & Jimenez 2006; Pujals *et al.* 2009), harmonic forcing (Hwang & Cossu 2010) or the resolvent analysis (McKeon 2017), is a method of qualitatively revealing the mechanisms of typical flow structures and the variation of their characteristics (Jiménez

2018; Marusic & Monty 2019). Applying these methods to the mean profiles of high-speed turbulent boundary layers, Alizard *et al.* (2015) and Dawson & McKeon (2020) found the weak compressibility effects on the characteristic length, the orientation angles and shapes of the non-modal optimal perturbations for both the inner and outer modes, corresponding to the velocity streaks in the buffer region and the VLSMs in the outer layer, respectively. The Reynolds number considered is restricted within a low level of $Re_\tau \lesssim 500$, indicating that no or weak VLSMs can be found. Similar conclusions were obtained in a recent study by Chen *et al.* (2023) in turbulent channels with a large parameter space covering various Reynolds and Mach numbers. However, as they have pointed out in the discussion, the conclusions obtained in this way are more qualitative than quantitative.

The lack of systematic knowledge of the Mach number effects on the VLSMs in moderate- and high-Reynolds-number turbulent boundary layers serves as the motivation for the present study. In this paper, we investigate the influences of the free stream Mach numbers on VLSMs by performing high-precision numerical simulations at $Re_\tau = 1000$ and M_∞ ranging from 2.0 to 5.0 (§ 2), orchestrating numerical experiments (§ 3) and theoretical analyses of turbulent kinetic energy production (§ 4). These methods provide evidence in different aspects to the conclusion that the VLSMs are weakened with the increment of Mach numbers, as summarized in § 5.

2. Observation: abatement of turbulent intensities and VLSMs

As a preliminary impression of the VLSMs, we first perform implicit large eddy simulation (LES) of turbulent boundary layers over adiabatic walls at the friction Reynolds number $Re_\tau \approx 1000$ and the free stream Mach number M_∞ ranging from 2.0 to 5.0, governed by the Navier–Stokes equations of perfect Newtonian gases. Hereinafter, the velocity in the x (streamwise), y (wall-normal) and z (spanwise) directions are represented by u, v and w, respectively. The density, pressure and temperature are denoted by ρ, p and T, related by the state equation of perfect gases. The viscous stresses and the heat transfer are obtained by the constitutive equations and Fourier's law of Newtonian fluids, with μ and κ being the viscosity and heat conductivity.

The simulation is performed in a rectangular box with the sizes of $(80, 9, 10)\delta_{in}$ in x, y and z directions, discretized by $(2400, 330, 600)$ grids in the three directions, with δ_{in} the nominal boundary layer thickness at the inlet of the computational domain. At the flow inlet, the synthetic turbulence is given by the recycling-rescaling method at the reference station $x = 53\delta_{in}$ (Pirozzoli, Bernardini & Grasso 2010). The no-slip and no-penetration for velocity and isothermal condition for temperature $T_w = T_r$ (T_r the recovery temperature at the given Mach number) are applied at the wall. The non-reflection conditions are enforced at the upper and outlet boundaries to eliminate the possible numerical errors that could contaminate the flow field within the computational domain. Periodic conditions are adopted in the spanwise direction.

The flow parameters are listed in table 1. The simulations are performed using the open-source code developed by Bernardini *et al.* (2021). The convective terms are approximated by the hybrid scheme, namely the low-dissipative sixth-order kinetic preserving scheme (Pirozzoli 2010) in the smooth region and the fifth-order weighted essentially non-oscillatory (WENO) scheme (Shu & Osher 1988) at the flow discontinuity detected by Ducro's sensor (Ducros *et al.* 1999). The viscous terms are expanded into the Laplacian form and then approximated by the sixth-order central scheme. The time advancement is achieved by the third-order low-storage Runge–Kutta scheme (Wray 1990). The subgrid stresses and heat fluxes are incorporated by the overly dissipative WENO scheme, thus no subgrid models are implemented (Kokkinakis & Drikakis 2015; Ritos

Cases	M_∞	Re_∞	Re_θ	Re_τ	T_w/T_∞	Δx^+	Δz^+	Δy_w^+
M2	2.0	64 425	5095	1031	1.71	19.4	9.7	0.78
M3	3.0	135 233	8391	1023	2.60	18.8	9.4	0.69
M4	4.0	250 714	12 316	987	3.85	18.5	9.3	0.70
M5	5.0	556 654	22 636	1014	5.46	22.6	8.9	0.60

Table 1. Flow parameters. Here, M_∞ is the free stream Mach number, Re_∞, Re_θ and Re_τ are the free stream, momentum and friction Mach number at the reference station. Additionally, T_w is the wall temperature and Δx_i is the mesh interval along the x_i coordinate.

et al. 2017). The simulations have been run for more than $500\delta/U_\infty$ before the collection of turbulent statistics, and another period of approximately $800\delta/U_\infty$ in each case for investigation. Herein, the boundary layer thickness δ is the off-wall distance where the mean velocity reaches 99 % of the free stream values. At the streamwise station with the friction Reynolds number Re_τ of approximately 1000, the grid resolution in the streamwise and spanwise directions are $\Delta x^+ \approx 20$ and $\Delta z^+ \approx 10$, and the first grid distance off the wall being $\Delta y_w^+ \approx 0.7$ (refer to table 1), satisfying the requirement of LES. Such a method has been proven to be capable of providing acceptable results under the presently considered Re_τ, grid intervals and numerical schemes (De Vanna *et al.* 2023).

In figure 1(*a*), we present the wall-normal distribution of the van Driest transformed mean velocity $\tilde{u}_{VD}^+$, with the symbol $\tilde{\cdot}$ denoting its density-weighted average, as well as those by Bernardini & Pirozzoli (2011) at $M_\infty = 2$ and $Re_\tau \approx 1000$ for comparison. The results of case M2 are generally consistent with the reference data across the boundary layer, suggesting the validity of the present numerical methods. For all the cases considered, the mean velocity obeys the linear law in the viscous sublayer and the logarithmic law within $y^+ = 30$ and $y = 0.3\delta$, but are lowered in the wake region with the rising Mach number. The density-weighted root-mean-square (r.m.s.) of velocity fluctuations u''^*_{rms} shown in figure 1(*b*) (with $\cdot''$ marking the fluctuations and the superscripts $*$ the non-dimensionalization as $u''_{rms}/\sqrt{\tau_w/\rho_w}$) also manifest considerable agreement with the reference. The u''^*_{rms} reaches the maximum at $y^+ \approx 12$ in the buffer layer, beyond which it gradually decays. Within a small range of $y^+ = 100 \sim 300$, the u''^*_{rms} decays logarithmically in each case (Marusic *et al.* 2013; Lozano-Durán & Jiménez 2014), but the slopes and intercepts of the logarithmic laws (if any) are different. There exhibits a monotonic abatement as the Mach number increases.

It is expected that the decrease of the fluctuation intensities with the Mach numbers in the outer layer above can be associated with the flow structures. As shown in figure 2(*a*), the low-speed regions in the instantaneous field reach higher wall-normal locations. The spanwise length scale of these velocity streaks within the buffer layer is estimated to be $100\delta_\nu$ (δ_ν is the viscous length scale) (Flores & Jiménez 2010; Hwang 2013; Yu, Xu & Pirozzoli 2019; Cogo *et al.* 2022) and that of the low momentum region in the outer region, known as the VLSMs, is approximately the boundary layer thickness δ (Hutchins & Marusic 2007; Jiménez 2018; Yu & Xu 2022; Yu *et al.* 2023). These energetic structures are manifested as the two peaks in the pre-multiplied spanwise spectra in figure 2(*b*) (Huang *et al.* 2022; Yu & Xu 2022). Qualitatively, the distributions of the spectra and instantaneous flow structures are marginally dependent on the Mach number. However, the specific values of the inner and outer peaks extracted from each spectra, as shown in figure 2(*c*), suggest that the velocity streaks in the inner region are slightly strengthened but the VLSMs in the outer regions are significantly weakened with the increment of the

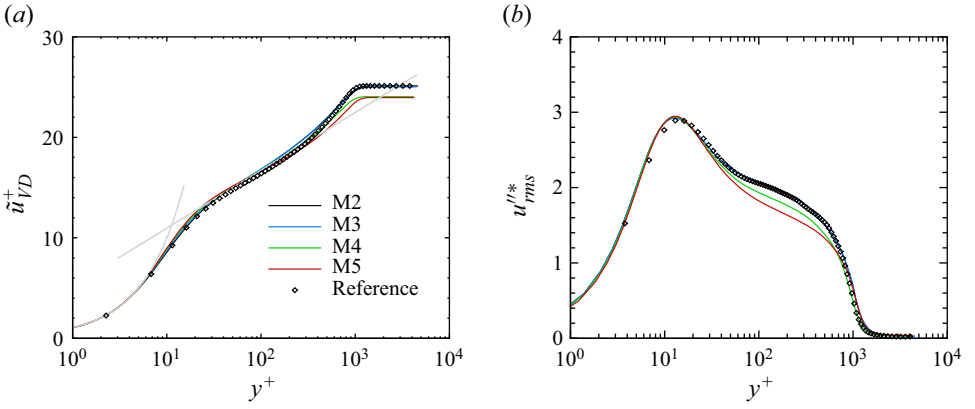

Figure 1. Wall-normal distribution of (*a*) van Driest transformed mean velocity $\tilde{u}^+_{VD}$ and (*b*) density-weighted r.m.s. of velocity fluctuations u''^*_{rms}. Reference: Bernardini & Pirozzoli (2011) at $M_\infty = 2$ and $Re_\tau = 1000$.

Mach number, as also indicated by the lower spectra intensity in the outer region shown in figure 2(*b*), consistent with the results reported by Cogo *et al.* (2022) and Huang *et al.* (2022).

Integrating the spanwise spectra gives the r.m.s. of the velocity fluctuations. The results are reported in figure 3, in which the large- and small-scale portions are separated by $\lambda_z = 0.5\delta$. Expectedly, the density-weighted r.m.s. of the small-scale velocity u'' is weakly dependent on the Mach number. They are also well-collapsed with the low-Reynolds-number statistics ($M_\infty = 2$, $Re_\tau = 250$) reported by Bernardini & Pirozzoli (2011) within $y^+ \approx 100$ where the VLSMs are absent, suggesting that the small-scale motions in the inner region are Mach number independent at the presently considered moderate Reynolds number and are statistically equivalent to the low-Reynolds-number turbulence. This is consistent with our previous findings with the aid of minimal flow units in turbulent channels (Yin, Huang & Xu 2017; Yu *et al.* 2023). The large-scale portion, however, manifests consistent decrement in magnitude with the Mach number. Based on the statistics above, the abatement of the velocity fluctuation u''^*_{rms} in the outer region should be ascribed to the weaker VLSMs in higher Mach number flows at the similar friction Reynolds number Re_τ. Notably, when normalized by their peak values at $y = 0.2\delta$, the profiles can be collapsed to a single curve in the inner region (inset of figure 3*b*), indicating that the superposition of the large-scale motions on the inner region (Mathis *et al.* 2009; Mathis, Hutchins & Marusic 2011) remains unaltered quantitatively.

3. Dynamic relevance: transient growth of streamwise rollers

We attempt to provide an explanation of the weakening of VLSMs by orchestrating numerical experiments for the inspection of the generation of the very-large-scale velocity streaks excited by the streamwise rollers, which are the optimal output and input (Hwang & Cossu 2010; McKeon 2017) or the optimal amplification and initial perturbations (Del Alamo & Jimenez 2006; Brandt 2014) obtained in linear stability analysis in wall-bounded turbulence (Alizard *et al.* 2015; Chen *et al.* 2023). Such a task requires the accurate distribution of the mean velocity and an initial perturbation. The former is obtained via the postulation that (i) the mean velocities are consistent with those of the incompressible flows, independent of Mach numbers and wall temperatures, by applying the following transformation to the mean velocity and the wall-normal coordinate proposed by Volpiani

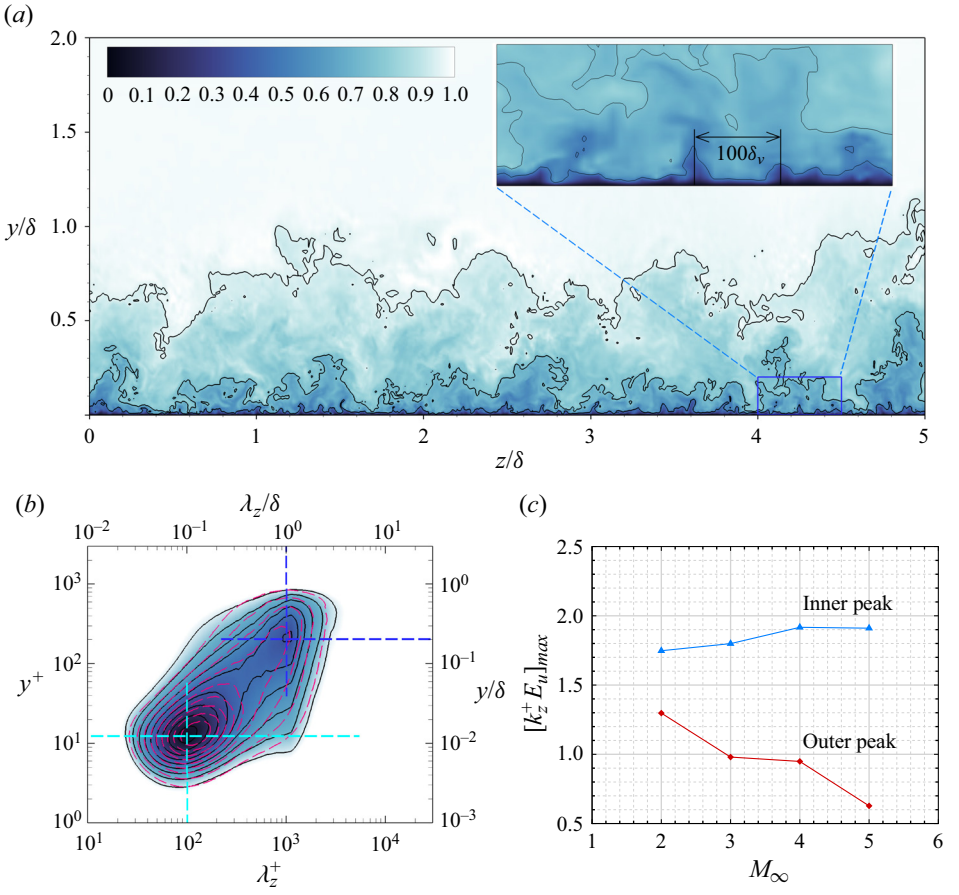

Figure 2. (*a*) Instantaneous streamwise velocity u/U_∞ in case M3, (*b*) the density-weighted spanwise spectra of case M3 (flooded and black solid lines) and of case M5 (red dashed lines), (*c*) the values of the inner and outer peaks at various Mach numbers.

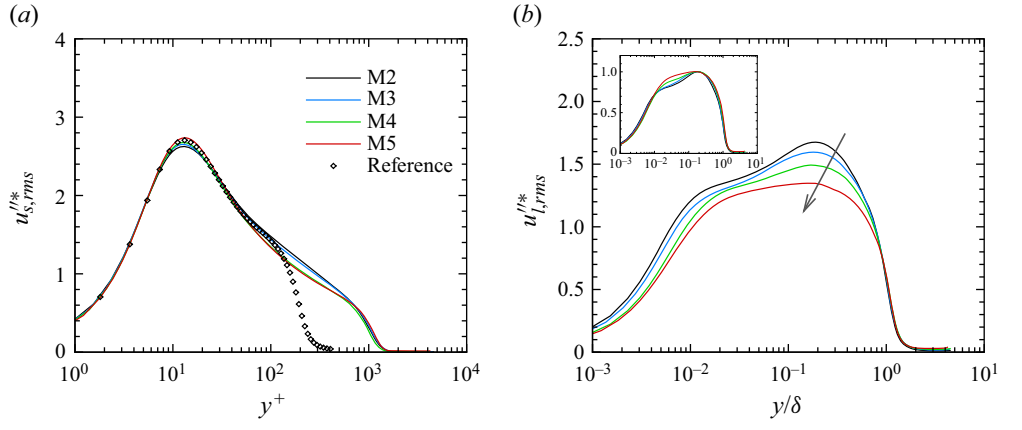

Figure 3. Density-weighted r.m.s. of u'': (*a*) small-scale portion $u''^*_{s,rms}$; (*b*) large-scale portion $u''^*_{l,rms}$, where the inset shows values normalized at $y = 0.2\delta$. Symbols in panel (*a*): Bernardini & Pirozzoli (2011) at $M_\infty = 2$ and $Re_\tau = 250$.

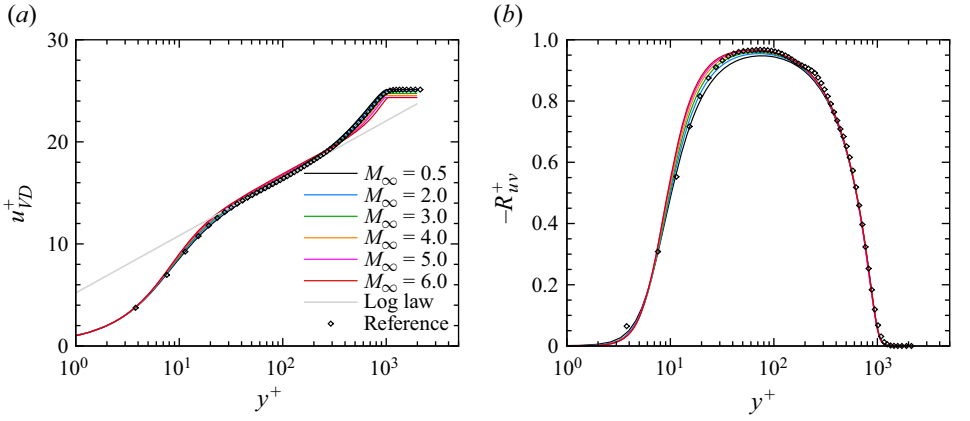

Figure 4. Wall-normal distribution of constructed (*a*) u^+_{VD} and (*b*) $-R^+_{uv}$. Symbols in panel (*a*): Bernardini & Pirozzoli (2011) at $M_\infty = 2$ and $Re_\tau = 1000$.

et al. (2020):

$$y^+_{VP} = \frac{1}{\delta_v}\int_0^y \sqrt{\frac{\bar\rho}{\bar\rho_w}\frac{\bar\mu_w^3}{\bar\mu^3}}\,\mathrm{d}y, \quad u^+_{VP} = \frac{1}{u_\tau}\int_0^{\tilde u}\left(\sqrt{\frac{\bar\rho}{\bar\rho_w}\frac{\bar\mu_w}{\bar\mu}}\right)\mathrm{d}\tilde u, \tag{3.1a,b}$$

and that (ii) the mean velocity of the incompressible turbulent boundary layers can be constructed as (Subrahmanyam, Cantwell & Alonso 2022)

$$\bar u^+(y^+) = \int_0^{y^+}\left[-\frac{1}{2\lambda(s)^2} + \frac{1}{2\lambda(s)^2}\left(1 + 4\lambda(s)^2\left(1 - \frac{s}{Re_\tau}\right)\right)^{1/2}\right]\mathrm{d}s, \tag{3.2}$$

in which the mixing-length function is expressed as

$$\lambda = \frac{ky^+(1 - \exp(-(y^+/a)^m))}{(1 + (y^+/(bRe_\tau))^n)^{1/n}} \tag{3.3}$$

with $k = 0.42$, $a = 24.96$, $m = 1.15$, $b = 0.18$ and $n = 2.17$. The total shear stress distribution is presumed to satisfy

$$\tau(y) = \bar\mu\frac{\partial\bar u}{\partial y} + R_{uv} = \tau_w(1 - \chi^{3/2}), \quad \chi = \frac{y/\delta}{(1 + (y/\delta)^p)^{1/p}}, \tag{3.4a,b}$$

with $p = 17$ to ensure that τ gradually decays to zero as it reaches the free stream (Chen & She 2016; Wang 2022). With the aforementioned information and the generalized Reynolds analogy (Zhang *et al.* 2014), the mean velocity can be readily obtained by setting the Mach number, wall temperature and the target friction Reynolds number. The constructed mean velocity and the Reynolds shear stress at $Re_\tau = 1000$, M_∞ ranging from 0.3 to 6.0 and $T_w = T_r$, as shown in figure 4, are well-collapsed with those reported by Bernardini & Pirozzoli (2011), particularly that at $M_\infty = 2.0$, suggesting the validity of the presently adopted methodology. Such a construction of the mean velocity and the Reynolds shear stress also shows considerable accuracy at lower Reynolds numbers, various Mach numbers and wall temperatures (Zhang, Duan & Choudhari 2018), which are omitted here for brevity.

According to the study by Alizard *et al.* (2015) and Dawson & McKeon (2020), the optimal initial perturbations are weakly dependent on Mach numbers. Therefore, the

initial perturbation in the form of streamwise vortices is generated using the following cross-stream velocity:

$$\left.\begin{aligned} v' &= A\exp(-(y/\delta)^2)\cos(2\pi z)\sin(2\pi\sqrt{y})/\sqrt{\bar{\rho}}, \\ w' &= A\exp(-(y/\delta)^2)\sin(2\pi z)\sin(2\pi\sqrt{y})/\sqrt{\bar{\rho}}, \end{aligned}\right\} \tag{3.5}$$

with the initial amplitude $A = 0.01U_\infty$ and the mean density divided so as to ensure that the turbulent kinetic energies of the initial perturbation are the same for cases at different Mach numbers.

The numerical simulations of this process are performed in rectangular boxes with the sizes of $(10, 3, 1)\delta$ and the periodic conditions in the streamwise and spanwise directions to obtain the temporal evolution of the initial perturbation. The mean profiles are enforced to remain steady at each step. In figure 5(*a*), we present the turbulent kinetic energy amplification of the streamwise velocity u' and cross-stream velocities v' and w', denoted by $G_u(t)$ and $G_{vw}(t)$, which are calculated by the ratio between the integrated energy of the corresponding velocity components in the computational domain and that of initial perturbations. For all the cases considered, the streamwise rollers (figure 5*b*, vectors) decay at the same rate, as can be inferred from their almost identical temporal evolution. These structures bring the low-speed fluids upwards and the high-speed fluids downwards, inducing the spanwise alternating structures resembling the VLSMs in moderate- and high-Reynolds-number flows. Intriguingly, the amplification of these large-scale streamwise velocity fluctuations $G_u(t)$ decreases with the Mach number, despite that the kinetic energy of initial perturbations is determined to be identical, and that the optimal growth rates are reached at the same time instant. Therefore, it can be concluded that the abatement of the streamwise velocity fluctuations should be attributed to the inherent properties of the flow dynamics that the perturbations of the same energy are only capable of triggering the VLSM structures with lower energy at higher Mach numbers, in accordance with the statistical results in § 2. The conclusion is the same by setting the initial perturbation with the same magnitude of velocity (without weighted by density in (3.5)) and momentum (divided by $\bar{\rho}$ in (3.5)). The results obtained in this way are qualitatively the same as those obtained in compressible turbulent channels by Chen *et al.* (2023) under the framework of linearized governing equations with harmonic and stochastic forcing.

4. Turbulent kinetic energy production

Inspecting the turbulent production term that extracts the kinetic energy from the mean flow to turbulent fluctuations is another possibly effective perspective for explaining the variation of turbulent kinetic energy at different flow parameters. One example would be that the increasing turbulent production in the outer region corresponds to the enhanced turbulent kinetic energy and prominent VLSMs centred at $y \approx 0.2\delta$ and that a long extending plateau in the logarithmic layer is manifested at sufficiently high Reynolds numbers (Marusic, Mathis & Hutchins 2010; Smits *et al.* 2011). According to its expression $P_K = R_{uv}\partial\bar{u}/\partial y$, the turbulent production term can be constructed once the mean velocity and the Reynolds shear stress are obtained from (3.1*a*,*b*)–(3.4*a*,*b*).

In figure 6(*a*), we present the distribution of P_K normalized by viscous scales and pre-multiplied by y^+ for a better representation of the integration against the logarithmic abscissa. The peaks in the outer region located at $y^+ \approx 400$ decrease monotonically to be manifested as a plateau at $M_\infty = 4.0$ and as a shoulder at $M_\infty > 5.0$. The conclusions remain valid when inspected by the LES results in § 2. This confirms our previous

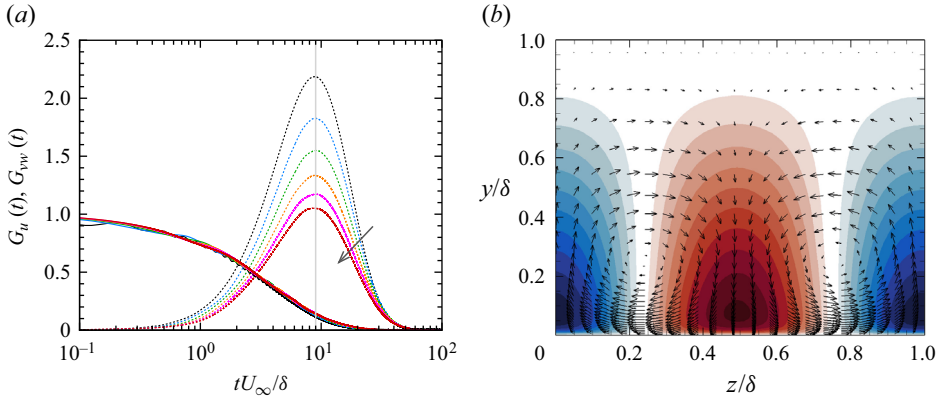

Figure 5. (*a*) Energy amplification of the initial perturbation in the form of streamwise vortices: solid, $G_{vw}(t)$; dotted, $G_u(t)$; line legends refer to figure 4. (*b*) Initial v' and w' perturbation (vector) and the u' at $t = 9\delta/U_\infty$ (flooded).

elucidations and postulations that the turbulent intensities are weakened by the higher Mach numbers. Such a variation can also be inferred by reformulating the production term as

$$P_K^+ = R_{uv}^+ \frac{\partial \bar{u}^+}{\partial y^+} = R_{uv}^+ \frac{\partial \bar{u}_{VD}^+}{\partial y^+} \sqrt{\frac{\bar{\rho}_w}{\bar{\rho}}} \approx R_{uv}^+ \frac{\partial \bar{u}_{VD}^+}{\partial y^+} \sqrt{\frac{\bar{T}}{T_w}}, \tag{4.1}$$

where the mean pressure across the boundary layer is presumed to be constant. Since we have shown in figure 4 that the van Driest transformed mean velocity $\bar{u}_{VD}^+$ and the Reynolds shear stress R_{uv}^+ are weakly dependent on the Mach number, the first two factors in the last expression of (4.1) should be regarded as invariants, leaving mean temperature variation as the only source of disparity. For high-speed turbulent boundary layers over adiabatic walls ($T_w = T_r$), it is well established that the ratio $\bar{T}/T_w$ decreases with the increment of Mach numbers at a certain off-wall location within the boundary layer. Henceforth, it is straightforward that the production term P_K^+, the rate of energy transfer from the mean to turbulent kinetic energy, is curtailed. Naturally, the profiles of the P_K^+ at various Mach numbers can be collapsed under the transformation proposed by Volpiani *et al.* (2020), but this means nothing, for the integration in the physical space (y/δ) is identical, irrelevant of the transformation adopted.

The method of construction of the turbulent production P_K^+ allows the exploration of turbulent characteristics without performing formidable and extravagant high-precision numerical simulations, especially when the Reynolds numbers are extremely high. Taking its advantage, we further discuss the influences of the other two parameters, i.e. the friction Reynolds number Re_τ and the wall temperature T_w.

In figure 6(*b*), we present the pre-multiplied turbulent production $y^+P_k^+$ at the Mach numbers of $M_\infty = 0.5$ and 6.0, and the wall temperature of $T_w = T_r$ (adiabatic), with the friction Reynolds number ranging from $Re_\tau = 500$ to 20 000. At the lower Mach number $M_\infty = 0.5$, the variation of $y^+P_k^+$ resembles that of the incompressible turbulent boundary layers in that the inner and outer peaks are gradually separated by a gradually elongated plateau in the logarithmic region. When it comes to high-Mach-number flows, however, the peaks and the plateau exist no more, merely manifesting longer ranges of logarithmic decay and small shoulder before they decrease abruptly to insignificant values. This suggests

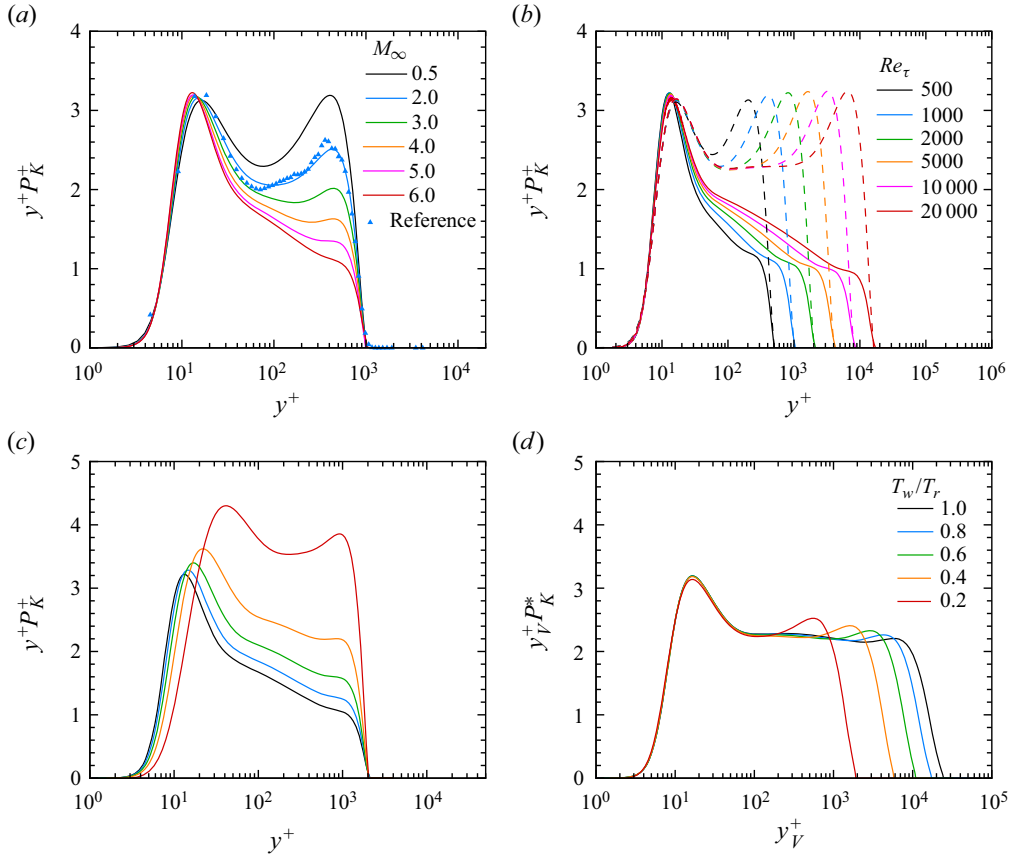

Figure 6. Wall-normal distribution of the pre-multiplied constructed turbulent production $y^+P_k^+$ at different (*a*) Mach numbers ($Re_\tau = 1000$, $T_w = T_r$), (*b*) Reynolds numbers ($T_w = T_r$, dashed, $M_\infty = 0.5$; solid, $M_\infty = 6.0$) and (*c*) wall temperatures ($Re_\tau = 2000$, $M_\infty = 6.0$), and (*d*) $y_V^+P_K^*$ normalized by semi-local scales, parameters are the same as those in panel (*c*). Symbols in panel (*a*): Bernardini & Pirozzoli (2011) at $M_\infty = 2$ and $Re_\tau = 1000$.

that the lower intensity of large- and very-large-scale turbulent structures and the turbulent intensities in the outer region are universal phenomena at all Reynolds numbers instead of a sporadic occurrence at certain combinations of flow parameters.

We also exploit the influences of the wall temperature by inspecting the production term P_K^+ at $M_\infty = 6$ and $Re_\tau = 2000$ with the wall temperature being $T_w = (1.0, 0.8, 0.6, 0.4, 0.2)T_r$. The results are shown in figure 6(*c*,*d*), normalized by viscous and semi-local scales, respectively. Expectedly, the turbulent production P_K^+ is well collapsed under the semi-local scaling (figure 6*d*) in the near-wall region and shows a long extending plateau in the log layer, resembling those of the incompressible flows. Nevertheless, such rescaled wall-normal coordinates are non-physical, as pointed out previously, for they are not uniformly transformed from the physical space, leading to the misconception of the wall temperature independence. When plotted against the viscous scales, as demonstrated in figure 6(*c*), the P_K^+ is augmented by the decreasing wall temperature, indicating that the cooling walls tend to enhance the large-scale motions in the outer region, at any rate in the perspective of kinetic energy transfer. However, the intervals between the two peaks (or the shoulders) are shortened, consistent with the DNS

results given by Huang *et al.* (2022), suggesting the smaller scale separation between the inner and outer motions (Smits *et al.* 2011). This has been verified to be consistent with the DNS results reported by Zhang *et al.* (2018) at $M_\infty \approx 6$ and $Re_\tau = 450$. The same conclusions can be drawn if transient growth of the large-scale streamwise rollers is used to investigate this issue, which is demonstrated in the Appendix.

To summarize, over adiabatic walls, the turbulent production term that represents the kinetic energy transfer from the mean to turbulent flows decreases monotonically with the increasing Mach number at all Reynolds numbers in the logarithmic and outer layers. At the same Re_τ and M_∞, the turbulent productions above the buffer region are gradually increased by the cooling walls. Although they only serve as qualitative indicators of the intensification or diminishment of VLSMs, these elucidations are consistent with the existing DNS or LES results.

5. Conclusions

In this study, we investigate the variation of very-large-scale motions (VLSMs) in supersonic and hypersonic turbulent boundary layers using large eddy simulations, well-constructed numerical experiments and theoretical analyses. Our findings indicate that the increment of free stream Mach numbers leads to the weaker VLSMs, which are characterized by streamwise elongated spanwise alternating low- and high-momentum regions. This conclusion is supported by the observed decrease in the intensity of spectra and turbulent fluctuations corresponding to large-scale motions, the reduction in amplifications of transient growth excited by streamwise rollers and the curtailment of the production of turbulent kinetic energy. Under hypersonic conditions, the cooling wall inclines to enhance the VLSMs in the outer region and reduce the scale-separation between the VLSMs and the small-scale structures close to the wall.

The numerical simulations performed in the present study only cover the range of moderate Reynolds numbers. Since the previous studies of Baars & Marusic (2020*a*,*b*) regarding the Reynolds number effects in incompressible turbulent boundary layers have shown that the intensities of the VLSMs are insensitive to the Reynolds number when they are split from the rest of the structures via the spectral linear stochastic estimation, we believe our conclusions can be applied to higher Reynolds number flows as well. However, concrete proof from numerical or experimental studies is required for validation, which will be carried out in our future work.

Funding. This work is supported by the National Natural Science Foundation of China (grant no. 12202469 and 92052301), the National Key R&D Program of China (grant no. 2019YFA0405201) and China Postdoctoral Science Foundation.

Declaration of interests. The authors report no conflict of interest.

Author ORCIDs.
Ming Yu https://orcid.org/0000-0001-7772-833X;
SiWei Dong https://orcid.org/0000-0002-4725-2964;
XianXu Yuan https://orcid.org/0000-0002-7668-0116;
ChunXiao Xu https://orcid.org/0000-0001-5292-8052.

Appendix. Transient growth of streamwise rollers at different wall temperature

To further validate the conclusion that the intensity of the VLSM is increased as the wall temperature becomes lower, we perform simulations following the method in § 3 to reveal the amplification of the large-scale streamwise velocity fluctuations induced

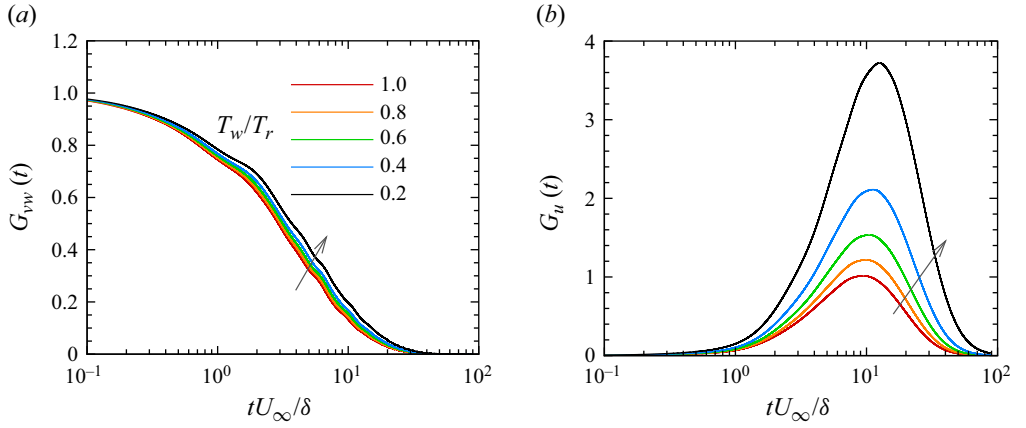

Figure 7. Energy amplification of the initial perturbation in the form of streamwise vortices, $M_\infty = 6$, $Re_\tau = 2000$, $T_w = (0.2 \sim 1.0)T_r$: (*a*) $G_{vw}(t)$; (*b*) $G_u(t)$.

by the large-scale streamwise rollers with the same initial kinetic energy. As discussed in § 4, we consider the hypersonic turbulent boundary layers at the friction Reynolds number $Re_\tau = 2000$, the free stream Mach number of $M_\infty = 6.0$ and the wall temperature $T_w = (1.0, 0.8, 0.6, 0.4, 0.2)T_r$. The amplification of the cross-stream and streamwise kinetic energies G_{vw} and G_u are shown in figure 7. With the decreasing wall temperature, the G_{vw} decays at a lower rate, leading to the slight tardiness of the attainment of the optimal u' disturbances. The peaks of G_u, however, are higher, suggesting the more intensified optimal u' disturbances and hence the stronger VLSMs. This is consistent with the conclusions in § 3 regarding the variation of VLSMs with the wall temperature.

References

Alizard, F., Pirozzoli, S., Bernardini, M. & Grasso, F. 2015 Optimal transient growth in compressible turbulent boundary layers. *J. Fluid Mech.* **770**, 124–155.

Baars, W.J. & Marusic, I. 2020*a* Data-driven decomposition of the streamwise turbulence kinetic energy in boundary layers. Part 1. Energy spectra. *J. Fluid Mech.* **882**, A25.

Baars, W.J. & Marusic, I. 2020*b* Data-driven decomposition of the streamwise turbulence kinetic energy in boundary layers. Part 2. Integrated energy and A_1. *J. Fluid Mech.* **882**, A26.

Bernardini, M., Modesti, D., Salvadore, F. & Pirozzoli, S. 2021 STREAmS: a high-fidelity accelerated solver for direct numerical simulation of compressible turbulent flows. *Comput. Phys. Commun.* **263**, 107906.

Bernardini, M. & Pirozzoli, S. 2011 Wall pressure fluctuations beneath supersonic turbulent boundary layers. *Phys. Fluids* **23** (8), 085102.

Brandt, L. 2014 The lift-up effect: the linear mechanism behind transition and turbulence in shear flows. *Eur. J. Mech. (B/Fluids)* **47**, 80–96.

Bross, M., Scharnowski, S. & Kähler, C.J. 2021 Large-scale coherent structures in compressible turbulent boundary layers. *J. Fluid Mech.* **911**, A2.

Chen, X. & She, Z.S. 2016 Analytic prediction for planar turbulent boundary layers. *Sci. China Phys. Mech.* **59**, 1–7.

Chen, X. & Sreenivasan, K.R. 2021 Reynolds number scaling of the peak turbulence intensity in wall flows. *J. Fluid Mech.* **908**, R3.

Chen, X.L., Cheng, C., Fu, L. & Gan, J.P. 2023 Linear response analysis of supersonic turbulent channel flows with a large parameter space. *J. Fluid Mech.* **962**, A7.

Cogo, M., Salvadore, F., Picano, F. & Bernardini, M. 2022 Direct numerical simulation of supersonic and hypersonic turbulent boundary layers at moderate-high Reynolds numbers and isothermal wall condition. *J. Fluid Mech.* **945**, A30.

DAWSON, S.T.M. & MCKEON, B.J. 2020 Prediction of resolvent mode shapes in supersonic turbulent boundary layers. *Intl J. Heat Fluid Flow* **85**, 108677.

DE VANNA, F., BALDAN, G., PICANO, F. & BENINI, E. 2023 Effect of convective schemes in wall-resolved and wall-modeled LES of compressible wall turbulence. *Comput. Fluids* **250**, 105710.

DEL ALAMO, J.C. & JIMENEZ, J. 2006 Linear energy amplification in turbulent channels. *J. Fluid Mech.* **559**, 205–213.

DUAN, L., BEEKMAN, I. & MARTIN, M. 2011 Direct numerical simulation of hypersonic turbulent boundary layers. Part 3. Effect of Mach number. *J. Fluid Mech.* **672**, 245–267.

DUAN, L., BEEKMAN, I. & MARTIN, M.P. 2010 Direct numerical simulation of hypersonic turbulent boundary layers. Part 2. Effect of wall temperature. *J. Fluid Mech.* **655**, 419–445.

DUCROS, F., FERRAND, V., NICOUD, F., WEBER, C., DARRACQ, D., GACHERIEU, C. & POINSOT, T. 1999 Large-eddy simulation of the shock/turbulence interaction. *J. Comput. Phys.* **152** (2), 517–549.

FLORES, O. & JIMÉNEZ, J. 2010 Hierarchy of minimal flow units in the logarithmic layer. *Phys. Fluids* **22** (7), 071704.

GANAPATHISUBRAMANI, B., CLEMENS, N.T. & DOLLING, D.S. 2006 Large-scale motions in a supersonic turbulent boundary layer. *J. Fluid Mech.* **556**, 271–282.

GRIFFIN, K.P., FU, L. & MOIN, P. 2021 Velocity transformation for compressible wall-bounded turbulent flows with and without heat transfer. *Proc. Natl Acad. Sci.* **118** (34), e2111144118.

HUANG, J., DUAN, L. & CHOUDHARI, M.M. 2022 Direct numerical simulation of hypersonic turbulent boundary layers: effect of spatial evolution and Reynolds number. *J. Fluid Mech.* **937**, A3.

HUANG, P.G., COLEMAN, G.N. & BRADSHAW, P. 1995 Compressible turbulent channel flows: DNS results and modelling. *J. Fluid Mech.* **305**, 185–218.

HUTCHINS, N. & MARUSIC, I. 2007 Evidence of very long meandering features in the logarithmic region of turbulent boundary layers. *J. Fluid Mech.* **579**, 1–28.

HWANG, Y. 2013 Near-wall turbulent fluctuations in the absence of wide outer motions. *J. Fluid Mech.* **723**, 264–288.

HWANG, Y.Y. & COSSU, C. 2010 Linear non-normal energy amplification of harmonic and stochastic forcing in the turbulent channel flow. *J. Fluid Mech.* **664**, 51–73.

JIMÉNEZ, J. 2018 Coherent structures in wall-bounded turbulence. *J. Fluid Mech.* **842**, P1.

KOKKINAKIS, I.W. & DRIKAKIS, D. 2015 Implicit large eddy simulation of weakly-compressible turbulent channel flow. *Comput. Meth. Appl. Mech. Engng* **287**, 229–261.

LEYVA, I.A. 2017 The relentless pursuit of hypersonic flight. *Phys. Today* **70** (11), 30–36.

LOZANO-DURÁN, A. & JIMÉNEZ, J. 2014 Effect of the computational domain on direct simulations of turbulent channels up to $Re_\tau = 4200$. *Phys. Fluids* **26** (1), 011702.

MARUSIC, I., MATHIS, R. & HUTCHINS, N. 2010 High Reynolds number effects in wall turbulence. *Intl J. Heat Fluid Flow* **31** (3), 418–428.

MARUSIC, I. & MONTY, J.P. 2019 Attached eddy model of wall turbulence. *Annu. Rev. Fluid Mech.* **51**, 49–74.

MARUSIC, I., MONTY, J.P., HULTMARK, M. & SMITS, A.J. 2013 On the logarithmic region in wall turbulence. *J. Fluid Mech.* **716**, R3.

MATHIS, R., HUTCHINS, N. & MARUSIC, I. 2009 Large-scale amplitude modulation of the small-scale structures in turbulent boundary layers. *J. Fluid Mech.* **628**, 311–337.

MATHIS, R., HUTCHINS, N. & MARUSIC, I. 2011 A predictive inner–outer model for streamwise turbulence statistics in wall-bounded flows. *J. Fluid Mech.* **681**, 537–566.

MCKEON, B.J. 2017 The engine behind (wall) turbulence: perspectives on scale interactions. *J. Fluid Mech.* **817**, P1.

MODESTI, D. & PIROZZOLI, S. 2016 Reynolds and Mach number effects in compressible turbulent channel flow. *Intl J. Heat Fluid Flow* **59**, 33–49.

MODESTI, D. & PIROZZOLI, S. 2019 Direct numerical simulation of supersonic pipe flow at moderate Reynolds number. *Intl J. Heat Fluid Flow* **76**, 100–112.

MODESTI, D., PIROZZOLI, S. & GRASSO, F. 2019 Direct numerical simulation of developed compressible flow in square ducts. *Intl J. Heat Fluid Flow* **76**, 130–140.

PIROZZOLI, S. 2010 Generalized conservative approximations of split convective derivative operators. *J. Comput. Phys.* **229** (19), 7180–7190.

PIROZZOLI, S. 2011 Numerical methods for high-speed flows. *Annu. Rev. Fluid Mech.* **43**, 163–194.

PIROZZOLI, S. & BERNARDINI, M. 2013 Probing high-Reynolds-number effects in numerical boundary layers. *Phys. Fluids* **25** (2), 021704.

PIROZZOLI, S., BERNARDINI, M. & GRASSO, F. 2010 Direct numerical simulation of transonic shock/boundary layer interaction under conditions of incipient separation. *J. Fluid Mech.* **657**, 361–393.

PUJALS, G., GARCÍA-VILLALBA, M., COSSU, C. & DEPARDON, S. 2009 A note on optimal transient growth in turbulent channel flows. *Phys. Fluids* **21** (1), 015109.

RITOS, K., KOKKINAKIS, I.W., DRIKAKIS, D. & SPOTTSWOOD, S.M. 2017 Implicit large eddy simulation of acoustic loading in supersonic turbulent boundary layers. *Phys. Fluids* **29** (4), 046101.

SEGALL, B.A., SHEKHTMAN, D., HAMEED, A., CHEN, J.H. & PARZIALE, N.J. 2023 Profiles of streamwise velocity and fluctuations in a hypersonic turbulent boundary layer using acetone tagging velocimetry. *Exp. Fluids* **64** (6), 122.

SHU, C.W. & OSHER, S. 1988 Efficient implementation of essentially non-oscillatory shock-capturing schemes. *J. Comput. Phys.* **77** (2), 439–471.

SMITS, A.J., MCKEON, B.J. & MARUSIC, I. 2011 High–Reynolds number wall turbulence. *Annu. Rev. Fluid Mech.* **43**, 353–375.

SUBRAHMANYAM, M.A., CANTWELL, B.J. & ALONSO, J.J. 2022 A universal velocity profile for turbulent wall flows including adverse pressure gradient boundary layers. *J. Fluid Mech.* **933**, A16.

THEOFILIS, V., PIROZZOLI, S. & MARTIN, P. 2022 Special issue on the fluid mechanics of hypersonic flight. *Theor. Comput. Fluid Dyn.* **36** (1), 1–8.

TRETTEL, A. & LARSSON, J. 2016 Mean velocity scaling for compressible wall turbulence with heat transfer. *Phys. Fluids* **28** (2), 026102.

TU, G., CHEN, J., YUAN, X., YANG, Q., DUAN, M., YANG, Q., DUAN, Y., CHEN, X., WAN, B. & XIANG, X. 2021 Progress in flight tests of hypersonic boundary layer transition. *Acta Mech. Sin.* **37** (11), 1589–1609.

VOLPIANI, P.S., IYER, P.S., PIROZZOLI, S. & LARSSON, J. 2020 Data-driven compressibility transformation for turbulent wall layers. *Phys. Rev. Fluids* **5** (5), 052602.

WANG, H.N. 2022 Fluctuation generation at inlet and off-wall boundaries for eddy-resolving simulation of wall turbulence (in mandarin). PhD thesis, Tsinghua University.

WILLIAMS, O.J.H., SAHOO, D., BAUMGARTNER, M.L. & SMITS, A.J. 2018 Experiments on the structure and scaling of hypersonic turbulent boundary layers. *J. Fluid Mech.* **834**, 237–270.

WRAY, A. 1990 Minimal storage time advancement schemes for spectral methods. Report No. MS 202, NASA Ames Research Center, California.

YAO, J. & HUSSAIN, F. 2020 Turbulence statistics and coherent structures in compressible channel flow. *Phys. Rev. Fluids* **5** (8), 084603.

YAO, J. & HUSSAIN, F. 2023 Study of compressible turbulent plane Couette flows via direct numerical simulation. *J. Fluid Mech.* **964**, A29.

YIN, G., HUANG, W. & XU, C. 2017 On near-wall turbulence in minimal flow units. *Intl J. Heat Fluid Flow* **65**, 192–199.

YU, M., FU, Y.L., TANG, Z.G., YUAN, X.X. & XU, C.X. 2023 Predicting near-wall turbulence with minimal flow units in compressible turbulent channel flows. *Chin. J. Aeronaut.* **36** (8), 24–31.

YU, M., LIU, P.X., FU, Y.L., TANG, Z.G. & YUAN, X.X. 2022*a* Wall shear stress, pressure and heat flux fluctuations in compressible wall-bounded turbulence. II. Spectra, correlation and nonlinear interactions. *Phys. Fluids* **34** (6), 065140.

YU, M., LIU, P.X., FU, Y.L., TANG, Z.G. & YUAN, X.X. 2022*b* Wall shear stress, pressure, and heat flux fluctuations in compressible wall-bounded turbulence. Part I. One-point statistics. *Phys. Fluids* **34** (6), 065139.

YU, M., XU, C. & PIROZZOLI, S. 2019 Genuine compressibility effects in wall-bounded turbulence. *Phys. Rev. Fluids* **4** (12), 123402.

YU, M. & XU, C.X. 2022 Predictive models for near-wall velocity and temperature fluctuations in supersonic wall-bounded turbulence. *J. Fluid Mech.* **937**, A32.

YU, M., XU, C.X. & PIROZZOLI, S. 2020 Compressibility effects on pressure fluctuation in compressible turbulent channel flows. *Phys. Rev. Fluids* **5** (11), 113401.

ZHANG, C., DUAN, L. & CHOUDHARI, M.M. 2018 Direct numerical simulation database for supersonic and hypersonic turbulent boundary layers. *AIAA J.* **56** (11), 4297–4311.

ZHANG, P.J.Y., WAN, Z.H., LIU, N.S., SUN, D.J. & LU, X.Y. 2022 Wall-cooling effects on pressure fluctuations in compressible turbulent boundary layers from subsonic to hypersonic regimes. *J. Fluid Mech.* **946**, A14.

ZHANG, Y., BI, W., HUSSAIN, F. & SHE, Z. 2014 A generalized Reynolds analogy for compressible wall-bounded turbulent flows. *J. Fluid Mech.* **739**, 392–420.